4 × 25 GHz uni-traveling carrier photodiode arrays monolithic with InP-based AWG demultiplexers using the selective area growth technique

Han Ye (叶 焓)[1], Qin Han (韩 勤)[1,2,*], Qianqian Lv (吕倩倩)[1], Pan Pan (潘 盼)[1], Junming An (安俊明)[1,3], Xiaohong Yang (杨晓红)[1,3], Yubing Wang (王玉冰)[1], and Rongrui Liu (刘荣瑞)[1]

[1]*State Key Laboratory of Integrated Optoelectronics, Institute of Semiconductors, Chinese Academy of Sciences, Beijing 100083, China*

[2]*School of Electronic, Electrical and Communication Engineering, University of Chinese Academy of Sciences, Beijing 100049, China*

[3]*College of Materials Science and Opto-Electronic Technology, University of Chinese Academy of Sciences, Beijing 100049, China*

**Corresponding author: hanqin@semi.ac.cn*

Received March 12, 2017; accepted May 18, 2017; posted online June 13, 2017

We use the selective area growth (SAG) technique to monolithically integrate InP-based 4-channel arrayed waveguide gratings (AWGs) with uni-traveling carrier photodiode arrays at the O-band. Two kinds of channel spacing demultiplexers of 20 nm and 800 GHz are adopted for potential 100 Gbps coarse wavelength division multiplexing and local area network wavelength division multiplexing systems, with an evanescent coupling plan to facilitate the SAG technique into device fabrication. The monolithic chips in both channel spacings exhibit uniform bandwidths over 25 GHz and a photodiode responsivity of 0.81 A/W for each channel, in agreement with the simulated quantum efficiency of 80%. Cross talk levels are below −20 dB for both channel spacing chips.

OCIS codes: 230.3120, 230.5170, 230.7380.
doi: 10.3788/COL201715.082301.

InP-based photonics integration is becoming a competitive candidate for realizing optical modules with enhanced functionality at a reduced cost, especially in optical communication systems, since the proposal of wavelength division multiplexing (WDM). In recent years, network traffic has raised demands for high capacity, high speed transmission systems. Optical transceivers over 100 Gbps are in great need for relaxing this urgency[1,2].

The arrayed waveguide grating (AWG) is one of the most useful (de)multiplexers and core devices in optical integration, especially in multichannel data transmission systems[3]. InP-based AWGs take advantage of the deep-ridge waveguide shape to achieve a small bending radius and polarization independence. AWGs at the O-band have been reported as a reference for potential monolithic integration in data centers[4]. From the perspective of the receiver end, monolithic integration of AWGs with photodiodes (PDs) will reduce the complexity of photoreceivers at a lower cost and power loss.

Modern epitaxial technology has encouraged InP-based monolithic integration to a whole new level with multiple emerging passive-active integration plans[5–7]. Selective area growth (SAG) is the most promising technique for providing the biggest flexibility in structure and doping design[8]. Correspondingly, it requires a higher regrowth technical level and a more careful structure design. So far, there have been reports on monolithic AWG-PIN arrays of 16 × 2.5[3] and 10 × 10 Gbps[1] transmission rates. The bandwidth per channel is still limited for high-speed applications.

A uni-traveling carrier (UTC) PD structure has been proposed to enhance bandwidth and linearity performances, which utilizes faster photogenerated electrons to mitigate the space-charge effect[9], and is still of interest. A modified UTC structure has been proposed to reduce the delay time of electrons[10,11] and a charge-compensated structure has also been reported for better linearity and saturation photocurrent[12].

In this Letter, we use the SAG technique to monolithically integrate InP-based AWGs with UTC-PD arrays at the O-band. An evanescent coupling plan with an optimized extended matching layer is adopted to facilitate the SAG technique into the device fabrication, while ensuring a high quantum efficiency of 80% at the same time. Both 4-channel AWG-PDs for coarse wavelength division multiplexing (CWDM) with a 20 nm channel spacing and local area network (LAN) WDM with an 800 GHz (~4.5 nm) channel spacing are designed and fabricated. The monolithic chips show uniformity and stability in PD performances that agree well with theory.

The butt-joint situation is shown in Fig. 1. The PD layers are grown directly on an AWG core layer in the first epitaxy process, as listed in Table 1, and the AWG top cladding layer is regrown in a second epitaxy. A distance of $L = 10$ μm is reserved intentionally between the PD

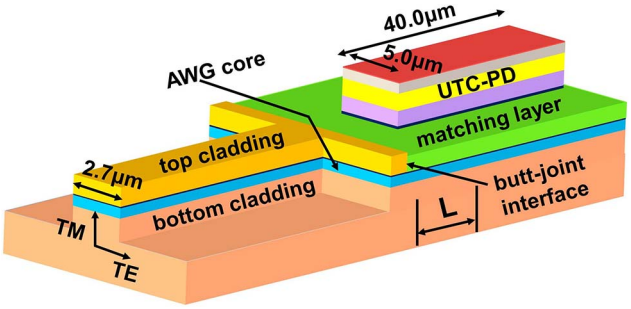

Fig. 1. Butt-joint situation of AWG-UTC chip.

mesa and butt-joint interface, connected by an extended matching layer for better optical coupling.

Quantum efficiency was simulated by increasing the distance between the waveguide and the PD mesa (L) for the butt-joint with and without the extended matching layer, as illustrated in Fig. 2, where the core layer in Fig. 2(a) was always fully covered by the matching layer but completely uncovered in Fig. 2(b). The quantum efficiency of the PD is calculated by the power percentage absorbed by the PD normalized to the mode source power. The power absorbed per unit volume by the PD absorber is decided by the real part of the divergence of the Poynting vector by the equation[13]

$$P_{\text{abs}} = -\frac{1}{2} \cdot \text{real}(\nabla \cdot \vec{P}), \tag{1}$$

where $\vec{P}$ is the Poynting vector, and the total absorbed power is obtained by integrating through the absorber of 5 μm × 40 μm × 0.59 μm.

As seen in Fig. 3, the quantum efficiency decreases slightly with increasing distance during the first 7.5 μm ($0 < L < 7.5$) and the last 10 μm ($15 < L < 25$) for the extended matching layer situation, and remains quite stable around 80%, even turning slightly upwards, for a 7.5 μm range in the middle. On the contrary, the very appearance of a naked core layer results in an immediate drop of efficiency to around 60% within only a 1 μm length, and a continuous drop of efficiency after. The sudden drop of efficiency comes from optical field scattering at the butt-joint interface. In consideration of fabrication compatibility, a distance (also matching the layer extension length) of 10 μm is decided for stable quantum efficiency under a large photolithographic error tolerance and a safe space for unavoidable abnormal growth at the interface.

The epitaxial structure was grown by metal organic chemical vapor deposition (MOCVD) on a semi-insulating InP substrate. Before SAG of the AWG top cladding layer, the 1.49 μm high PD mesa was etched down to the matching layer by the inductively coupled plasma (ICP) technique. This step was intentionally prior to SAG for complete individualism of the PDs, so that each PD in the array would be electrically isolated from the others. The matching layer at the AWG region was then removed by a selective chemical solution of $H_2SO_4/H_2O_2/H_2O$, with a 300 nm SiO_2 protection mask covering the PD area and aligned at a 10 μm distance before the PD mesa. A large area (more than 7 times the PD area), 1.2 μm thick un-doped InP top cladding layer was then grown selectively by MOCVD at 610°C for 30 min. At the butt-joint interface, as in Figs. 4(a) and 4(b), an overgrown abnormal ridge with 4.67 μm width and 3.80 μm height was formed on the mask upon the matching layer. Due to the abnormal crystal quality and unrepeatable size of this ridge, it is difficult to remove this high ridge completely without damaging the AWG top cladding layer. This is also why the extended matching layer is necessary for pulling the PD mesas away and preventing overgrowth on the PD mesas. The mask was cleaned off after regrowth with a buffered oxide etchant to eliminate small crystalline grains on it, yet the ridge remained unaffected. Then the PD structure was accomplished by consecutive steps of N mesa etching to unintentionally doped (U.I.D) layers under the core layer with a bromine solution, SiO_2 passivation by plasma enhanced chemical vapor deposition (PECVD), and metallization

Table 1. Epitaxial Structure Before Regrowth.

Composition	Thickness (nm)	Doping	n@1310 nm	Function
$In_{0.53}Ga_{0.47}As$	30	P^+	3.65-i0.148	p-contact
InP	300	P^+	3.21	Electron blocker
$In_{0.53}Ga_{0.47}As$	590	P, graded	3.65-i0.148	Absorber
InGaAsP (Q1.24)	40	N^-	3.42	Cliff layer
InGaAsP (Q1.24)	430	U.I.D	3.42	Collector
InP	100	N	3.21	Dopant blocker
InGaAsP (Q1.24)	500	N^+	3.42	Matching layer
InP	150	U.I.D	3.21	Etch stop
InGaAsP (Q1.05)	500	U.I.D	3.298	AWG core
InP	1000	U.I.D	3.21	Bottom cladding

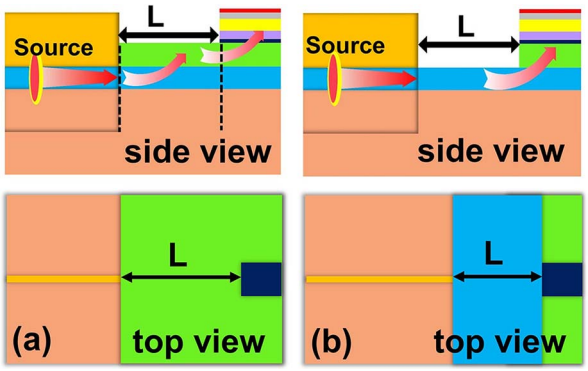

Fig. 2. Butt-joint (a) with and (b) without the extended matching layer.

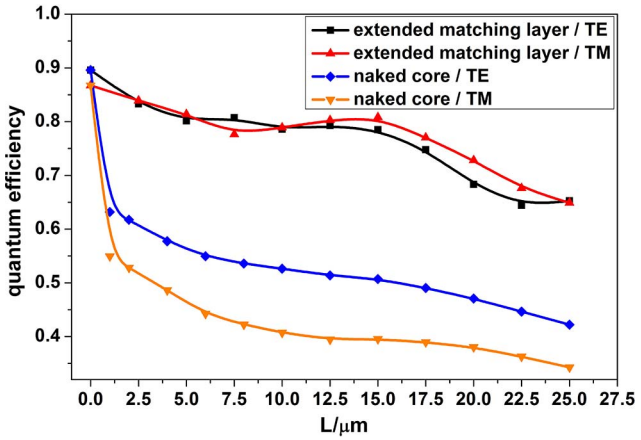

Fig. 3. (Color online) Simulated quantum efficiency of the PD with increasing distance between the butt-joint interface and the PD mesa.

with an Au/Ge/Ni alloy for N-contact and Ti/Au for P-contact, respectively. The AWG structure was finished at last by ICP etching while the PD area was protected by SiO_2, and the deep-ridge waveguide of 4.7 μm × 2.7 μm is shown in Fig. 4(c). A scanning electron micrograph (SEM) of the PD with the AWG cleaved off is also shown in Fig. 4(d). The total sizes of the AWG-UTC arrays are 4.5 mm × 1.2 mm for the 20 nm channel spacing and 4.5 mm × 1.67 mm for the 800 GHz channel spacing chips, as shown in Fig. 5.

Spectral photoresponses of the monolithic chips were measured by dividing the PD photocurrents from each channel by the fiber output power at the AWG input end (i.e., the to-fiber responsivity at the center wavelength, denoted by R). The unit A/W of the to-fiber responsivity is converted into dB in Figs. 6 and 7. The center wavelengths of the 20 nm channel spacing AWG are 1347.0, 1325.0, 1308.0, and 1286.5 nm, with a full width at half-maximum (FWHM) of 8.5 ± 0.5 nm, and cross talk below −22 dB. The 800 GHz channel spacing AWG exhibits 6 center wavelengths for each channel at the whole O-band due to a small free spectral range of 16.6 ± 1.2 nm. Taking the four wavelengths at 1296.8,

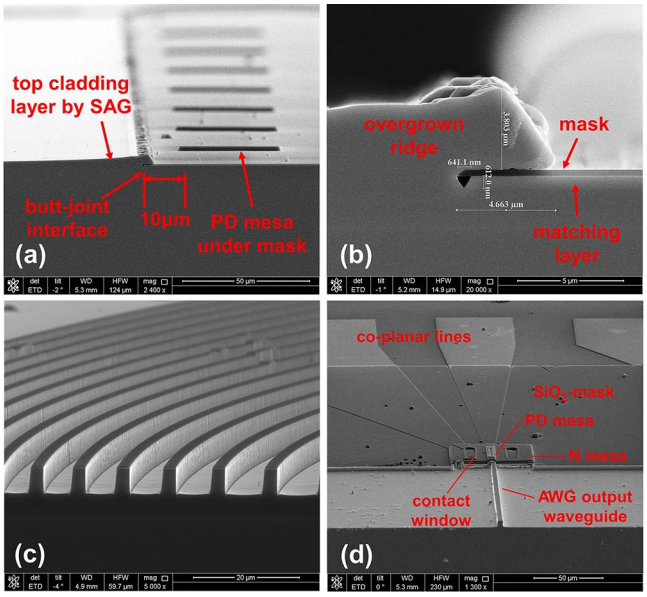

Fig. 4. SEMs in device fabrication with (a): the butt-joint interface after SAG; (b): the overgrown ridge at the interface; (c): deep-ridge etched arrayed waveguides; (d): the PD after the AWG is cleaved off.

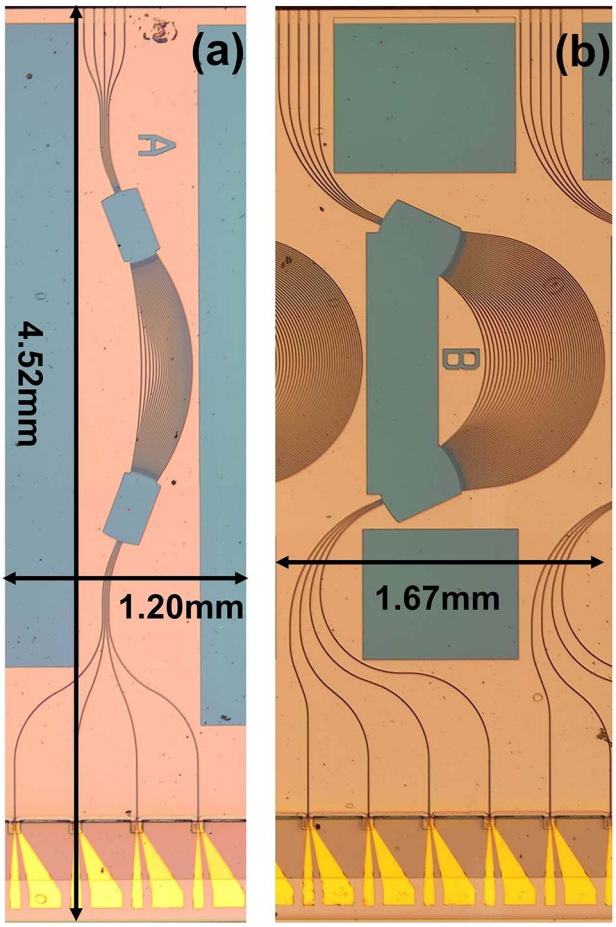

Fig. 5. Top views of the (a) 20 nm and (b) 800 GHz channel spacing AWG-UTC chips.

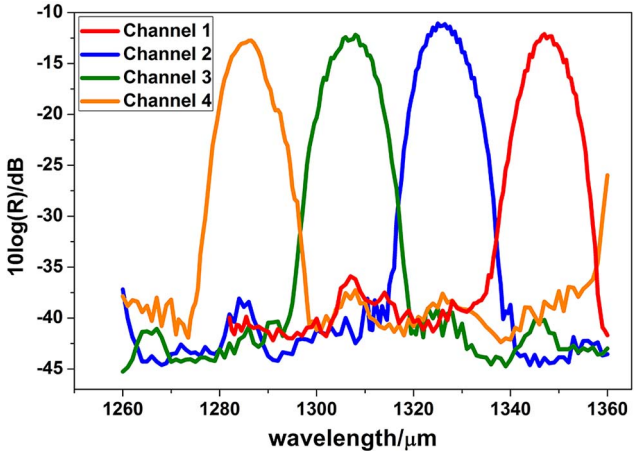

Fig. 6. (Color online) Spectral photoresponse of the 20 nm channel spacing AWG-UTC chip.

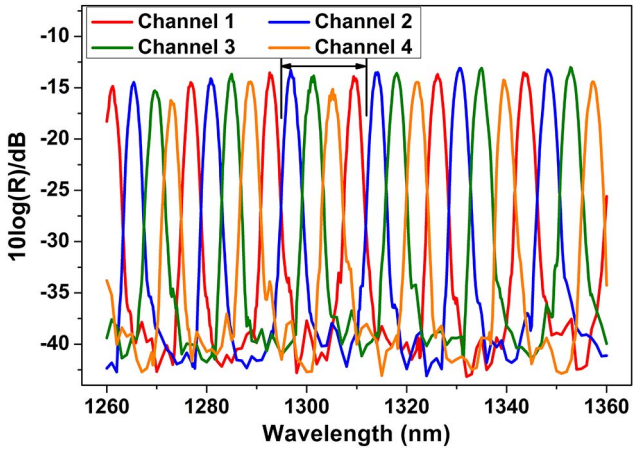

Fig. 7. (Color online) Spectral photo-response of the 800 GHz channel spacing AWG-UTC chip.

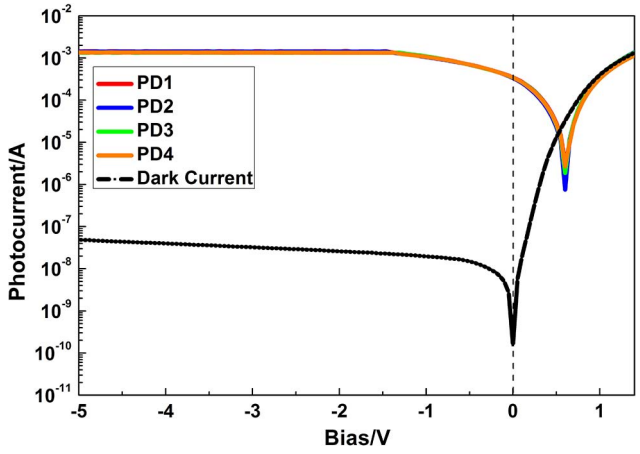

Fig. 8. (Color online) Photocurrents of the PDs without the AWG.

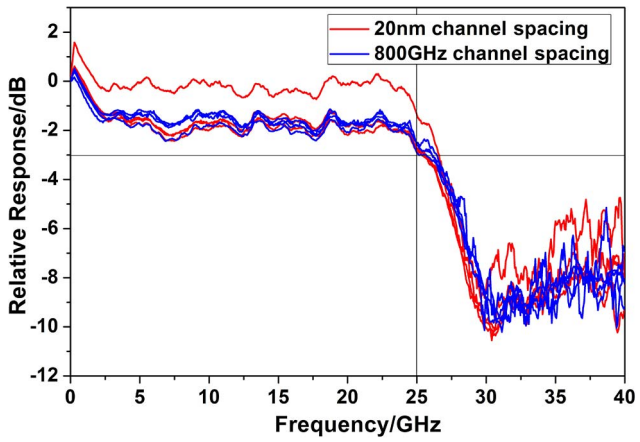

Fig. 9. (Color online) Bandwidth results for the AWG-UTC chips.

1301.4, 1305.2, and 1309.4 nm, the measured FWHM is 2.1 ± 0.1 nm, with cross talk below −20 dB.

We further cleaved AWGs off the chips, and measured the responsivity from the input end of the cleaved 185 μm output waveguide (WG) as in Fig. 4(d). To-WG responsivity includes (tapered) fiber-WG coupling loss into the PD responsivity, and remains uniformly around 0.28 A/W for both channel spacing devices. Photocurrents, e.g., for the 20 nm channeling spacing chip, under a 5 mW fiber output at −3 V are shown in Fig. 8. By deducting the to-WG responsivity from the to-fiber responsivity, the AWG on-chip loss is calculated to be −5.44 dB for the 20 nm channel spacing chip and −7.75 for the 800 GHz channel spacing chip.

The PD responsivity is obtained by further deducting the fiber-WG coupling loss from the to-WG responsivity. A typical loss of −4.6 dB was measured by using a short straight waveguide of the same end size with the AWG and halving the total loss from fiber-WG-fiber transmission. The PD responsivity then adds to the 0.81 A/W, corresponding to a quantum efficiency of 76.7% at 1310 nm, which agrees with the 80% simulated value.

The frequency responses of the PD arrays in both channel spacing chips were measured and are shown in Fig. 9. Each of the 4 channels for both kinds uniformly exceed a 25 GHz bandwidth at −3 V, which benefits from the pre regrowth etching of the PD mesas. The bandwidth is co-determined by the electron transit time in the UTC-PD and RC constant, as calculated by

$$f_t = \frac{1}{2\pi} \cdot \left(\frac{W_a}{2.8 v_{e-\mathrm{abs}}} + \frac{W_c}{2.8 v_{e-\mathrm{col}}} \right)^{-1}, \tag{2}$$

$$f_{\mathrm{RC}} = \frac{1}{2\pi (R_S + R_L) C} = \frac{1}{2\pi (R_S + R_L)} \cdot \frac{W_c}{\varepsilon_r \varepsilon_0 A}, \tag{3}$$

$$f_{-3\mathrm{dB}} = \left(f_t^{-2} + f_{\mathrm{RC}}^{-2} \right)^{-1/2}, \tag{4}$$

where f_t and f_{RC} are the transit-time-limited bandwidth and RC-limited bandwidth, respectively. W_a represents

the absorber thickness (590 nm), W_c is the depleted region thickness, D_e is the electron diffusion coefficient in p-InGaAs, v_{th} is the electron thermal emission velocity, $v_{e-\text{col}}$ is the electron velocity in the collector (2.5×10^7 cm/s), R_S is the series resistance (80 Ω in this work), R_L is the load resistance (50 Ω), C is the junction capacitance of the PD, ε_0 and ε_r (13.27) is the vacuum and relative dielectric constants, and A is the area of the PD depletion region (200 μm^2)[14,15]. Due to the graded doping profile and a consequent small quasi-electric field we adopted in p-absorber, the electron diffusion time in Ref. [14] is replaced by a drift time in Eq. (2). Furthermore, the cliff layer at the absorber-collector boundary also greatly reduces the delay time. Therefore, we consider the electron drift times in the absorber and depleted region as the primary sources of the transit time.

We take $W_c = 570$ nm as the sum of the collector and dopant blocker thicknesses as an approximation, and an electron velocity of 2.0×10^7 cm/s in the InGaAs. The calculated transit-time-limited bandwidth is 85.2 GHz. Together with the calculated RC bandwidth of 29.7 GHz, the −3 dB bandwidth then is added up to 28.0 GHz. The measured bandwidths agree well with the theoretical value, which also indicates a possible further improvement if the series resistance and junction capacitance are reduced. A response drop is observed at the initial low frequency, which may be attributed to a slight impedance mismatch. This could be eliminated by further careful electrical optimization.

In conclusion, we demonstrate the monolithic integration of 4-channel InP-based AWGs with UTC PD arrays in the O-band at 20 nm and 800 GHz channel spacings by the SAG technique. An evanescent coupling plan with an optimized 10 μm extended matching layer is adopted to offset abnormal regrowth after SAG, which ensures fabrication compatibility, and uniformly high bandwidth and PD responsivity of 25 GHz and 0.81 A/W for each channel in both channel spacing devices. Both measured results are in good agreement with theory and the overall 100 GHz is adequate to 10 km fiber-optic transmission by the 40GBASE-LR4 standard and 40 km transmission by the 100GBASE-ER4 standard. Compared with the previously reported device bitrates of 2.5 Gbps in Ref. [3] and 10.0 Gbps in Ref. [1], our device shows a good bandwidth advantage in the higher-speed systems nowadays.

This work was supported by the National High-Tech Research and Development Program of China (No. 2015AA016902) and the National Natural Science Foundation of China (Nos. 61635010, 61674136, and 61435002).

References

1. F. A. Kish, D. Welch, R. Nagarajan, J. L. Pleumeekers, V. Lal, M. Ziari, A. Nilsson, M. Kato, S. Murthy, P. Evans, S. W. Corzine, M. Mitchell, P. Samra, M. Missey, S. DeMars, R. P. Schneider, M. S. Reffle, T. Butrie, J. T. Rahn, M. Van Leeuwen, J. W. Stewart, D. J. H. Lambert, R. C. Muthiah, H.-S. Tsai, J. S. Bostak, A. Dentai, K.-T. Wu, H. Sun, D. J. Pavinski, J. Zhang, J. Tang, J. McNicol, M. Kuntz, V. Dominic, B. D. Taylor, R. A. Salvatore, M. Fisher, A. Spannagel, E. Strzelecka, P. Studenkov, M. Raburn, W. Williams, D. Christini, K. J. Thomson, S. S. Agashe, R. Malendevich, G. Goldfarb, S. Melle, C. Joyner, M. Kaufman, and S. G. Grubb, IEEE J. Sel. Top. Quantum Electron. **17**, 1470 (2011).
2. Z. Zhao, Y. Liu, Z. Zhang, X. Chen, J. Liu, and N. Zhu, Chin. Opt. Lett. **14**, 120603 (2016).
3. Y. Yoshikuni, IEEE J. Sel. Top. Quantum Electron. **8**, 1102 (2002).
4. P. Pan, J. M. An, Y. Wang, J. S. Zhang, L. L. Wang, Y. Qi, Q. Han, and X. W. Hu, Opt. Laser Technol. **75**, 177 (2015).
5. L. A. Coldren, S. C. Nicholes, L. Johansson, S. Ristic, R. S. Guzzon, E. J. Norberg, and U. Krishnamachari, J. Lightwave Technol. **29**, 554 (2011).
6. K. A. Williams, E. A. J. M. Bente, D. Heiss, Y. Jiao, K. Lawniczuk, X. J. M. Leijtens, J. J. G. M. van der Tol, and M. K. Smit, Photon. Res. **3**, B60 (2015).
7. L. Han, S. Liang, H. Zhu, and W. Wang, Chin. Opt. Lett. **13**, 081301 (2015).
8. M. Smit, X. Leijtens, H. Ambrosius, E. Bente, J. van der Tol, B. Smalbrugge, T. de Vries, E.-J. Geluk, J. Bolk, R. van Veldhoven, L. Augustin, P. Thijs, D. D'Agostino, H. Rabbani, K. Lawniczuk, S. Stopinski, S. Tahvili, A. Corradi, E. Kleijn, D. Dzibrou, M. Felicetti, E. Bitincka, V. Moskalenko, J. Zhao, R. Santos, G. Gilardi, W. Yao, K. Williams, P. Stabile, P. Kuindersma, J. Pello, S. Bhat, Y. Jiao, D. Heiss, G. Roelkens, M. Wale, P. Firth, F. Soares, N. Grote, M. Schell, H. Debregeas, M. Achouche, J.-L. Gentner, A. Bakker, T. Korthorst, D. Gallagher, A. Dabbs, A. Melloni, F. Morichetti, D. Melati, A. Wonfor, R. Penty, R. Broeke, B. Musk, and D. Robbins, Semicond. Sci. Technol. **29**, 083001 (2014).
9. T. Ishibashi, S. Kodama, N. Shimizu, and T. Furuta, Jpn. J. Appl. Phys. **36**, 6263 (1997).
10. D.-H. Jun, J.-H. Jang, I. Adesida, and J.-I. Song, Jpn. J. Appl. Phys. **45**, 3475 (2006).
11. Z. Li, H.-P. Pan, H. Chen, A. Beling, and J. C. Campbell, IEEE J. Quantum Electron. **46**, 626 (2010).
12. T. Shi, B. Xiong, C. Sun, and Y. Luo, Chin. Opt. Lett. **9**, 082302 (2011).
13. https://kb.lumerical.com/en/layout_analysis_pabs_simple.html.
14. H. Ito, S. Kodama, Y. Muramoto, T. Furuta, T. Nagatsuma, and T. Ishibashi, IEEE J. Sel. Top. Quantum Electron. **10**, 709 (2004).
15. S. Adachi, *Physical Properties of III-V Semiconductor Compounds: InP, InAs, GaAs, GaP, InGaAs, and InGaAsP* (Wiley, 1992), Chap. 8.